Research Square

Preprints are preliminary reports that have not undergone peer review.
They should not be considered conclusive, used to inform clinical practice,
or referenced by the media as validated information.

Finite Element and Machine Learning-Based Multi-Objective Prediction of Flexural Capacity and Crack Width for UHPC-Concrete Composite Beams

Jianan Qi

JN_Qi88910163.com

School of Civil Engineering, Southeast University

Jinxiao Mao

PetroChina Kunlun City Gas Company Limited Jiangsu Branch

Research Article

Keywords: Ultra-high-performance concrete (UHPC), Composite beams, Machine learning, Interpretability (SHAP), Finite element analysis

Posted Date: November 20th, 2026

DOI: https://doi.org/10.21203/rs.3.rs-11604939/v1

License: This work is licensed under a Creative Commons Attribution 4.0 International License.
Read Full License

Additional Declarations: No competing interests reported.

Finite Element and Machine Learning-Based Multi-Objective Prediction of Flexural Capacity and Crack Width for UHPC-Concrete Composite Beams

Abstract

To address computational complexity and lack of model transparency in predicting the performance of ultra-high-performance concrete (UHPC)-concrete composite beams, a framework integrating high-fidelity finite element (FE) modeling with interpretable machine learning is proposed. A verified 3D nonlinear FE model was combined with Python secondary development to construct a 420-case full-factorial dataset. Comparative analysis demonstrates that the Extreme Gradient Boosting (XGBoost) model delivers superior multi-objective accuracy. On the independent test set, root mean square errors for ultimate capacity (P_u) and maximum crack width ($w_{\max}$) were constrained to 6.45 kN and 0.012 mm ($R^2 > 0.968$), outperforming traditional empirical formulas and design codes. Furthermore, the SHapley Additive exPlanations (SHAP) framework was introduced to unbox the model. Global feature attribution identifies UHPC layer thickness (h_u) as the dominant factor in serviceability crack control, with a relative importance rate of 42.5%. Feature interaction analysis quantitatively reveals that increasing h_u from 30 mm to 90 mm induces an exponential crack width reduction of 60.5%–72.1%, self-consistent with classical damage mechanics. This study provides a precise and transparent digital tool for designing novel composite structures.

Keywords: Ultra-high-performance concrete (UHPC); Composite beams; Machine learning; Interpretability (SHAP); Finite element analysis

1 Introduction

Modern transportation infrastructure is developing toward long spans and lightweight designs, which poses severe challenges to the load-carrying capacity and long-term durability of modern engineering structures. Traditional reinforced concrete (RC) structures are limited by large self-weight, low tensile strength, and high susceptibility to cracking during the service period [1], resulting in severe steel corrosion that restricts their application in special-type structures [2]. Ultra-high-performance concrete (UHPC), characterized by ultra-high compressive and tensile strengths, high fracture toughness, and excellent durability, provides a breakthrough to overcome the performance bottlenecks of traditional structures [3, 4]. However, due to the high initial material cost, the full-section application of UHPC components lacks economic feasibility in large-scale projects [5]. In this context, UHPC-concrete composite beams have been developed [6]. In this structure, conventional concrete in the compression zone is utilized to bear compressive loads, while the high strength, toughness, crack resistance, and tensile potential of local UHPC in the tensile zone are released. Consequently, a significant leap in mechanical performance is achieved under the premise of substantially reducing material costs [7, 8]. A deep investigation into the flexural service characteristics, damage evolution laws, and flexural crack control behavior of this novel composite structure is of great theoretical value and engineering significance for enriching the calculation theory of hybrid bi-material structures and promoting the lightweight development of high-performance bridges [9].

Multi-dimensional exploration has been conducted by researchers worldwide regarding the

flexural behavior of UHPC-concrete composite beams. At the physical experimental level, the regulatory effect of the local UHPC layer on the full-service lifespan of composite beams has been systematically revealed through flexural tests, which confirms that the initial flexural stiffness, ultimate load capacity, and ductile deformation mode of the components can be significantly enhanced [10-12]. At the numerical simulation and theoretical analysis levels, existing studies have mostly focused on the strain compatibility laws of composite cross-sections [13], the characteristics of post-cracking stress redistribution [14], and the shear slip degradation behavior at the bi-material interface [15]. Extensive nonlinear finite element analysis (FEA) simulations indicate that the bond shear stiffness and strength of the interlaminar interface are the core links determining the perfect synergistic flexural action of composite beams [16]. However, the entire failure process of composite beams—from matrix initial cracking and steel reinforcement yielding to the crushing of conventional concrete in the compression zone—is accompanied by the alteration of multi-axial complex stress fields and localized discontinuous material transitions. Consequently, traditional analytical calculations of cross-sectional stiffness and ultimate load capacity are extremely complicated and difficult to balance with accuracy [17].

Under the serviceability limit state (SLS), the maximum crack width on the tensile side is the core indicator for evaluating the durability of UHPC-concrete composite beams [18]. Compared with ultimate load capacity prediction, the prediction of crack width for composite beams exhibits higher strong nonlinearity and coefficient of variation. This is mainly because the chopped steel fibers uniformly distributed inside the UHPC provide a strong fiber bridging effect after matrix cracking [19]. Due to this cracking mitigation mechanism, the failure mode at the bottom of the beam evolves from the single wide and deep main crack pattern of conventional concrete into multiple diffuse fine micro-cracks characteristic of UHPC [20]. Currently, specific formulas for crack calculation in such heterogeneous double-layer composite beams are still lacking in engineering design codes. The general practice is to reasonably extend the semi-empirical crack control models of traditional ordinary RC structures [21]. However, these traditional code formulas (such as GB 50010, ACI 318, and Eurocode 2) are derived based on simplified phenomenological theories, and their mathematical structures are fixed a priori. Consequently, the tensile hardening and fiber pull-out softening characteristics under micro-scale fiber sliding cannot be dynamically captured, and the intense coupling interactions among macro-scale features, such as UHPC layer thickness, longitudinal reinforcement ratio, and shear span-to-depth ratio, cannot be effectively processed [22]. As a result, systematic overestimation and distortion with excessive conservatism are easily generated by traditional code formulas in the micro-cracking region with small crack widths, which restricts the optimal design of novel composite structures [23].

In recent years, data-driven machine learning (ML) algorithms, such as XGBoost, random forest, and artificial neural networks, have demonstrated great application potential in predicting the performance of civil engineering structures due to their excellent advantages in high-dimensional nonlinear feature mapping [24, 25]. However, when ML algorithms are applied to the multi-objective and high-precision prediction of the ultimate load capacity and maximum crack width of UHPC-concrete composite beams, existing studies face two prominent technical bottlenecks. The first is the typical challenge of small sample limitations. Physical experiments are often accompanied by high time and economic costs, leading to an extreme scarcity of composite beam test samples available for extraction in currently published literature. Consequently, the data space required for training ML models cannot be satisfied, which easily triggers severe generalization

overfitting [26, 27]. The second is the inherent black-box defect of ML algorithms. Traditional ML tends toward pure numerical mapping, and the complex nested splitting structure inside the algorithms lacks physical transparency [28]. Due to this fitting mechanism that lacks physical mechanisms, the prediction laws of the models cannot be intuitively trusted by engineers, which seriously hinders the translational application of data-driven models in practical engineering safety assessment and code design [29, 30].

To address the aforementioned limitations, a closed-loop research framework consisting of a high-fidelity finite element (FE) extended dataset and interpretable machine learning (ML) multi-objective prediction is proposed in this study to overcome the challenges of complex calculation and algorithm opacity. Based on an FE model verified by physical experiments, a high-quality database with 420 samples was constructed via Python secondary development, based on which XGBoost, random forest, and artificial neural network models were evaluated for predicting the ultimate load capacity and maximum crack width. By comparing the optimized ML model with mainstream design codes across the test set, the calculation distortion boundaries and over-conservative defects of traditional formulas under complex conditions were quantitatively revealed. Furthermore, the SHAP framework was introduced for the first time to break the algorithm black box. Without prescribing any a priori mechanical equations, physical laws highly consistent with classical damage mechanics were spontaneously captured by the model, quantitatively elucidating the critical mechanisms of the shear span-to-depth ratio, concrete strength bottlenecks, and UHPC crack mitigation. This study provides a precise and transparent digital tool for the efficient and low-carbon design of novel composite structures.

2 Finite Element Simulation of UHPC-Concrete Composite Structures

2.1 Geometric Model and Boundary Conditions

To ensure the convergence and computational efficiency of the numerical simulation, the geometric configuration and boundary constraints of the finite element model (FEA) were meticulously designed and scientifically simplified in this study. This was conducted to satisfy the requirements for subsequent Python-based parametric batch calculations.

2.1.1 Geometric Dimension Design and 3D Solid Modeling

A double-layer composite simply supported beam was taken as the analysis object in this study, and its geometric configuration is shown in **Fig. 1**. The total length of the beam is $L = 2000$ mm, the computational span is $L_0 = 1800$ mm, the cross-sectional width is $b = 150$ mm, and the total cross-sectional height is $h = 300$ mm. The cross-section along the height direction consists of two parts: the upper part is the conventional concrete layer with a height of $h - h_u$, and the lower tensile zone is the high-toughness UHPC layer with a parametric variable height of h_u.

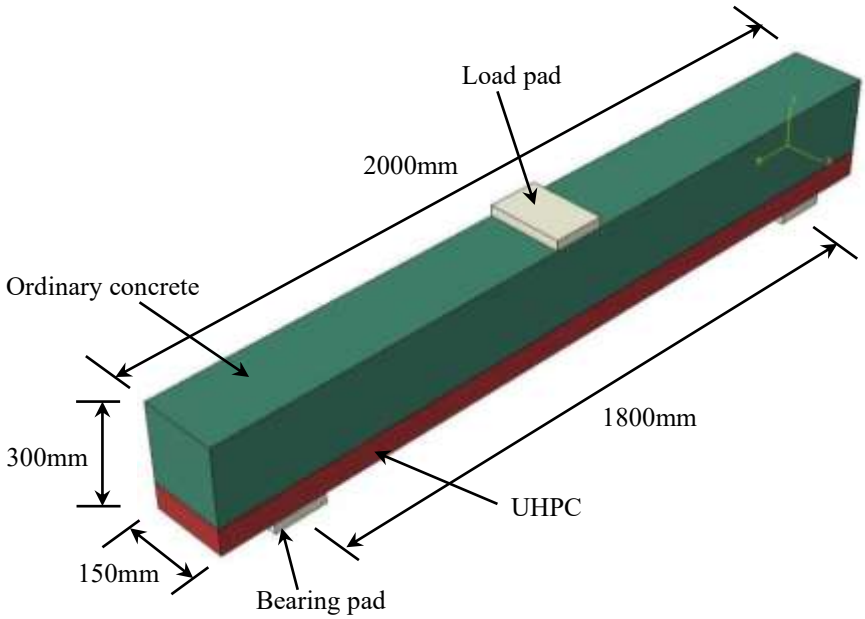

Fig. 1 Modelling of uhpc-concrete composite beams

The longitudinal tensile steel reinforcements inside the beam are symmetrically arranged at the bottom of the UHPC layer, and the distance from the center of gravity of the longitudinal reinforcements to the bottom of the beam is fixed at 25 mm. The reinforcement ratio ρ_s is controlled by automatically adjusting the reinforcement diameters ($d = 12,16,20,22$ mm). Two constructional erection bars with a diameter of 8 mm are arranged at the top of the compression zone. To prevent localized shear or bearing crushing failure, double-leg stirrups with a diameter of 8 mm and a spacing of 100 mm are arranged across the entire span of the beam.

In Abaqus, the conventional concrete layer and the UHPC layer were independently modeled using three-dimensional eight-node reduced-integration solid elements (C3D8R) to avoid shear locking and ensure computational accuracy under large deformations. The internal steel reinforcement skeleton was uniformly simulated using three-dimensional two-node linear truss elements (T3D2). A shared-nodes alignment design was adopted for the mesh at the bi-material interface to prevent stress transmission distortion caused by mismatched mesh sizes on the contact surface.

2.1.2 Boundary Constraints and Load Application Mechanisms

To eliminate stress concentration at the supports and loading points and to prevent element distortion, rigid steel pads (150 mm $\times$ 80 mm $\times$ 20 mm) were set at both the beam bottom supports and the beam top loading points, which were simulated using rigid body elements.

The global boundary constraints of the composite beam are defined as follows: at the simply supported end (left support reference point), translational displacements in three directions are restricted, namely $U_x = U_y = U_z = 0$; at the roller support end (right support reference point), vertical and transverse displacements are restricted, namely $U_y = U_z = 0$, while sliding along the beam axis (X direction) is allowed. Meanwhile, an out-of-plane displacement constraint ($U_z = 0$) is applied to the longitudinal symmetry plane of the entire beam to prevent out-of-plane lateral deflection or torsional instability during the full-service flexural process.

Displacement control is adopted for load application. A vertically downward displacement load of $U_y = -35$ mm is applied through the reference point of the rigid pad at the top of the mid-span.

Compared with force control, displacement control can achieve stable convergence in the full nonlinear static analysis, thereby fully capturing the full-service load-deformation curve, including the post-yield softening segment.

2.2 Compressive and Tensile Constitutive Relationships and Damage Evolution

The accurate definition of non-linear material constitutive relationships and physical damage evolution is a decisive factor for the finite element simulation to reproduce the entire process of structural bending. In this section, the concrete damaged plasticity (CDP) model for conventional concrete, the tensile and compressive constitutive relationships for UHPC, and the elastoplastic model for steel reinforcements are described.

2.2.1 Concrete Damaged Plasticity (CDP) Model for Ordinary Concrete

For the conventional concrete in the compression zone, the CDP model based on continuum mechanics and isotropic elastic damage theory is adopted in this study, and its core plasticity parameters are shown in **Table 1** [31,32]. To resolve the convergence challenges caused by highly nonlinear softening, a viscosity regularization parameter of $\mu = 0.0005$ is introduced. Consequently, the convergence of the implicit solver is improved under the premise of ensuring computational accuracy.

Table 1 Plastic calculation parameters of the CDP model for ordinary concrete

Plastic parameter	Dilation angle ψ (°)	Eccentricity ϵ	Biaxial/uniaxial strength ratio f_{b0}/f_{c0}	Second stress invariant ratio K_c	Viscosity parameter μ
Value	36	0.1	1.16	0.667	0.0005

2.2.2 Material Constitutive and Fiber Bridging Softening Model for Ultra-High-Performance Concrete (UHPC)

Due to the cracking mitigation effect of the internal high-density matrix and the high volume fraction (2%) of chopped steel fibers, UHPC exhibits high uniaxial compressive strength, as well as significant tensile strain hardening and crack bridging softening characteristics.

A tri-linear constitutive model is adopted for its uniaxial compression [33]. The stress remains in a perfectly elastic stage before reaching $0.6f_{cu}$ (with an elastic modulus of $E_u = 45$ GPa). Subsequently, the stress enters an ultimate hardening stage up to the peak compressive strength f_{cu}, where the strain reaches ε_{cu0}. After the peak, a compressive softening stage is entered. Due to the lateral restraint provided by the steel fibers, a high residual strength is still maintained even when the matrix is completely crushed at the ultimate compressive strain ε_{cu}.

A tensile strain hardening-strain softening bi-linear constitutive model is adopted for the uniaxial tension of UHPC. The stage before initial cracking (tensile stress $< f_{t0}$) is the elastic stage. After initial cracking, a strain hardening stage is entered, where the load transmission via fiber bridging across the cracks triggers dense and diffuse micro-cracks, and the stress continuously climbs to the ultimate tensile strength f_{ut} (ultimate tensile strain $\varepsilon_{ut} \geq 0.2\%$). After the strain exceeds ε_{ut}, a main crack is formed, progressive pulling out of the steel fibers occurs, and the fiber pull-out softening stage is entered. The relationship between the traction force and the crack opening displacement in this stage is expressed as:

$$\sigma_t(w) = f_{ut} \cdot \left(1 - \frac{w}{w_c}\right)^p \tag{1}$$

where w is the crack opening displacement; w_c is the critical crack width at which the steel fibers are completely pulled out and detached (taken as 3.0 mm); and p is the softening index (taken as 1.2). During the calculation, w is divided by the characteristic element length l_e to be converted

into the equivalent plastic tensile strain, which is then introduced into the CDP model. Consequently, a high-fidelity representation of the fiber-bridging crack mitigation behavior is achieved.

2.2.3 Elastoplastic Constitutive Model for Steel Skeleton

A bi-linear elastoplastic hardening model is uniformly adopted for the internal longitudinal reinforcements, erection bars, and stirrups of the composite beams. The mechanical properties are symmetric in tension and compression, satisfying the Von Mises yield criterion and the isotropic hardening law. The elastic modulus is set as $E_s = 2.0 \times 10^5$ MPa, and the Poisson's ratio is $\nu = 0.3$. After reaching the yield strength f_y (400 MPa for HRB400 and 500 MPa for HRB500), the hardening stage is entered with a hardening modulus of $E'_s = 0.01E_s = 2000$ MPa. This is utilized to account for the strain hardening effect in the large deformation stage, ensuring that a stable tensile increment can still be provided after crossing the peak load [34].

2.3 Coupling Constraints for Steel Skeleton and Interfacial Interface

The contact behavior at the internal steel skeleton-concrete matrix interface and the UHPC-conventional concrete bi-material interface inside the composite beams is the physical core determining the global stiffness degradation and deformation compatibility.

For the internal steel skeleton, the embedded region constraint method is adopted in this study to embed the steel truss elements as a whole into the solid elements of conventional concrete and UHPC. Full deformation compatibility between the reinforcements and the surrounding matrix is assumed by this method (perfect bond without relative slip). Since extremely high bond strength is possessed by the UHPC in the tensile zone and sufficient anchorage length is provided for the longitudinal steel reinforcements, pull-out slipping of the main reinforcements usually does not occur during flexural failure. Therefore, high macro-flexural prediction accuracy can be maintained by the embedded region constraint while computational efficiency is balanced.

Aiming at the characteristics of weak bond strength, high susceptibility to interlaminar delamination, and relative slip at the physical casting interface between the UHPC layer and the conventional concrete layer, a contact interaction based on cohesive behavior is defined between the contact surfaces of the two solid element layers in this study [35]. The nominal stress criterion is adopted by the cohesive model to determine the damage initiation of the interface. The traction-separation law in the normal and shear directions is expressed as:

$$\left\{\frac{\langle t_n \rangle}{t_n^0}\right\}^2 + \left\{\frac{t_s}{t_s^0}\right\}^2 + \left\{\frac{t_t}{t_t^0}\right\}^2 = 1 \tag{2}$$

where t_n, t_s, and t_t are the nominal tensile stresses of the interface in the normal and two shear directions, respectively; t_n^0, t_s^0, and t_t^0 are the ultimate bond strengths of the interface in each direction (set as 2.5 MPa and 4.0 MPa, respectively); and $\langle \cdot \rangle$ represents the Macaulay brackets, indicating that compressive stress does not induce normal tensile damage.

Once the multi-axial stress state of the interface satisfies the above equation, bond degradation of the interface begins (damage initiation), and the shear stiffness is subsequently reduced. The delamination phenomenon between the two material layers caused by the failure of matrix compatible deformation in the late stage of loading can be realistically reproduced by this refined simulation of interfacial slip. Consequently, high-fidelity displacement field and strain field data are provided for the subsequent precise extraction of cracking deformation and crack widths.

2.4 Mesh Division and Convergence Analysis

This section aims to determine the optimal mesh size for the parametric simulation. Based on a typical working condition ($h_u = 50$ mm, $\rho_s = 1.6\%$, $f_{cu} = 150$ MPa, $f_c = 40$ MPa, and $\bar{\lambda} =$

2.8) as the benchmark, four types of characteristic element size schemes were designed: 40 mm (Mesh-40), 20 mm (Mesh-20), 10 mm (Mesh-10), and 5 mm (Mesh-5).

The comparison of computational efficiency and load-carrying capacity accuracy under different mesh sizes is shown in **Table 2**. The load-carrying capacity calculated by the Mesh-40 scheme is 231.5 kN. Due to the stiffness hardening error induced by the overly coarse elements, the capacity is overestimated by 9.82% compared with that of the extremely fine mesh (Mesh-5, 210.8 kN). When the mesh size is refined to 20 mm, the load-carrying capacity converges to 213.2 kN, and the relative error compared with the benchmark value is only 1.14%, indicating that a substantial convergence of the spatial discretization error has been achieved.

Furthermore, when the mesh is refined from Mesh-20 to Mesh-5, the CPU calculation time for a single case surges from 210 s to 18,600 s, whereas the deviation in load-carrying capacity is only reduced by 1.14%. Considering the prediction accuracy, crack capture quality, and efficiency of large-sample parametric calculation comprehensively, 20 mm was selected as the standard mesh size in this study.

Table 2 Comparison of computational efficiency and load-carrying capacity accuracy for different mesh schemes

Mesh scheme	Characteristic size (mm)	Total number of elements	Ultimate load capacity P_u (kN)	Relative deviation (%)	Average CPU time per case (s)
Mesh-40	40	2,250	231.5	9.82%	45
Mesh-20	20	18,000	213.2	1.14%	210
Mesh-10	10	144,000	211.5	0.33%	2,450
Mesh-5	5	1,152,000	210.8	Base value	18,600

2.5 Experimental Verification of the Finite Element Model

To verify the reliability of the established three-dimensional nonlinear finite element (FE) model and the 20 mm mesh discretization benchmark, the numerical simulation results are cross-checked with published classical physical test data of simply supported beams under bending in this section [36]. By selecting two representative physical working conditions covering different UHPC layer thicknesses and reinforcement ratios, a high-standard verification is conducted from the two key dimensions of the macro-flexural path and the accuracy of the ultimate load capacity.

2.5.1 Parameter Selection of Verification Experimental Conditions

The specific design characteristics of the two groups of physical experimental verification conditions introduced in this study include the measured material strength, specimen geometric dimensions, steel skeleton spacing, and three-point bending boundary conditions. In Abaqus, full-scale numerical models were established strictly based on these physical indicators. The material constitutive relationships and interfacial contact of the models were implemented using the mechanical frameworks constructed in Sections 2.2 and 2.1, respectively. The detailed design parameters of the two working conditions are summarized in **Table 3**.

Table 3 Summary of material and geometric design parameters for experimental verification conditions

Case No.	Physical feature description of working condition	UHPC layer thickness h_u (mm)	Longitudinal reinforcement ratio ρ_s (%)	Ordinary concrete compressive strength f_c (MPa)	UHPC compressive strength f_{cu} (MPa)	Experimental design shear span-to-depth ratio $\bar{\lambda}$

EXP-1	Low reinforcement ratio and thin UHPC layer condition	35	1.2	35.6	138.5	3
EXP-2	High reinforcement ratio and thick UHPC layer condition	75	2.4	42.1	145.2	3

2.5.2 Comparison of Macro Load-Displacement Flexural Paths

The cross-comparison between the simulated mid-span flexural load-displacement curves and the physical test curves is shown in **Fig. 2**. The analysis indicates that the three mechanical characteristic stages during the full-service life of the composite beams under bending can be perfectly captured by the FEA model. In the elastic stage, the slopes of the simulated and experimental curves (initial flexural stiffness) at the early stage of loading overlap highly, which proves that the element mesh discretization and the initial elastic modulus values are precise. As the displacement advances into the cracking transition stage, the bottom of the beam reaches the elastic tensile limit of the UHPC, and a slight transition occurs in the curves. In this stage, a smooth stiffness degradation without sudden stress drops is exhibited by the simulated curves, which verifies that the bridging toughness of the steel fibers in the micro-cracking region is accurately captured by the tensile strain hardening constitutive relationship. After the yielding of the main reinforcements, the yielding and hardening stage is entered, and the slope of the curves slows down significantly. Benefiting from the synergy between the elastoplastic hardening constitutive relationship of the steel bars and the fiber pull-out softening model of the UHPC, the simulated curves climb smoothly to the peak point, and an excellent parallelism with the experimental paths is maintained.

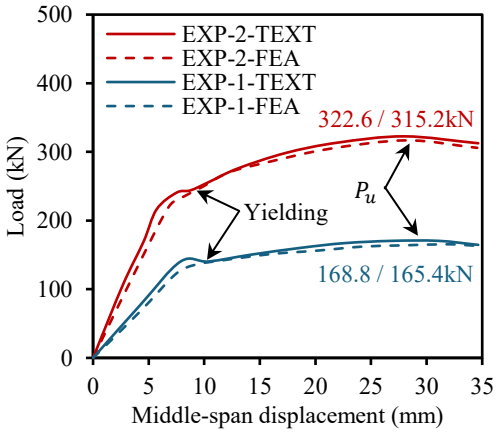

Fig. 2 Comparison of mid-span load-displacement verification curves between finite element simulation and physical experiments

Regarding the absolute value of the ultimate flexural capacity P_u, extremely high accuracy is demonstrated by the FEA model. For the EXP-1 condition, the experimental capacity is 165.4 kN, the simulated value is 168.8 kN, and the relative error is +2.06%. For the EXP-2 condition with more complex force states, the experimental value is 315.2 kN, the simulated value is 322.6 kN, and the relative error is +2.35%. The errors of both working conditions are far below the engineering acceptance threshold of 5%. The quantitative index calibration fully solidifies the data foundation for the subsequent large-sample parametric analysis. The detailed quantitative comparison and the summary of the final failure modes are presented in **Table 4**.

Table 4 Quantitative comparison indicators of ultimate load capacity and stiffness between finite element simulation and physical experiments

Case No.	Experimental ultimate capacity $P_{u,\mathrm{EXP}}$ (kN)	Simulated ultimate capacity $P_{u,\mathrm{FEA}}$ (kN)	Relative error of capacity (%)	Relative error of elastic stiffness (%)	Failure mode
EXP-1	165.4	168.8	2.06%	1.85%	Yielding of tensile steel bars - Crushing of ordinary concrete
EXP-2	315.2	322.6	2.35%	3.12%	Yielding of tensile steel bars - Crushing of ordinary concrete

3 Finite Element Simulation Results and Dataset Construction

3.1 Parametric Scheme Design and Dataset Construction

To overcome the bottlenecks of limited physical test samples and high acquisition costs, large-sample parametric numerical simulations were conducted in this study using the experimentally verified three-dimensional nonlinear finite element (FE) model. Based on the secondary development of Abaqus using Python, an automated closed-loop operation including geometric reconstruction, adaptive mesh division, material constitutive assignment, boundary application, job submission, and data extraction was achieved through self-written parametric modeling and post-processing scripts. Consequently, a solid data foundation was laid for constructing a prediction model with high generalization capability.

Closely incorporating the flexural capacity failure mechanism and crack evolution laws of UHPC-concrete composite beams, five design parameters with a decisive influence on the structural load-carrying characteristics were screened out as input features in this study. The UHPC layer thickness (h_u) directly regulates the cross-sectional flexural stiffness and the neutral axis position. The longitudinal tensile reinforcement ratio (ρ_s) is the core reinforcement indicator that regulates the capacity increment and crack control characteristics. The UHPC axial compressive strength (f_{cu}) and the ordinary concrete axial compressive strength (f_c) reflect the material constitutive levels of the matrices in the tensile and compression zones, respectively. The shear span-to-depth ratio ($\bar{\lambda}$) is utilized to control the influence of the combined flexural-shear action on the ultimate failure modes and crack distribution patterns of the composite beams. A full-factorial grid combination design was performed on the aforementioned five parameters in this study (as shown in **Table 5**), and a total of 432 numerical analysis working conditions were planned to comprehensively cover common engineering design variations.

Table 5 Independent variables and level design for parametric analysis

Independent variable	Physical meaning	Unit	Levels	Total number of levels
h_u	UHPC layer thickness	mm	30, 50, 70, 90	4
ρ_s	Longitudinal tensile reinforcement ratio	%	1.0%, 1.6%, 2.2%, 2.8%	4
f_{cu}	UHPC axial compressive strength	MPa	120, 150, 180	3
f_c	Ordinary concrete axial	MPa	30, 40, 50	3

	compressive strength			
$\bar{\lambda}$	Shear span-to-depth ratio	-	2.0, 2.8, 3.6	3

For each finite element case that completed calculation, the field output and history output in the output database of each working condition were automatically read by the post-processing script, and two key target responses were extracted. The ultimate flexural capacity (P_u) was extracted by tracing the peak load on the displacement-force curve at the loading reference point. The maximum physical crack width ($w_{\max}$) was evaluated by integrating the localized tensile plastic strain fields across the crack bandwidth. To eliminate the multi-microcracking pseudo-strain during UHPC tension-hardening, the residual fracture strain was calculated by deducting the elastic threshold (ε_{el}) and micro-crack saturation strain (ε_{sat}) from the total strain:

$$w_{\max} = \left(\varepsilon_t^{pl} - \varepsilon_{sat}\right) \cdot l_e \tag{3}$$

where $l_e = 20$ mm represents the characteristic element length under isotropic mesh discretization."

During the full-process automated operation, 12 groups of abnormal data caused by non-convergence of localized contact, calculation divergence due to large boundary deformations, or extreme mesh distortion were automatically identified and eliminated by the system. Consequently, a complete dataset containing 420 groups of effective response samples was successfully constructed. **Table 6** shows the input parameters and simulated output results of the first 15 groups of typical working conditions in the dataset. Preliminary analysis of the data characteristics indicates that an increase in the UHPC thickness and longitudinal reinforcement ratio can not only significantly enhance the ultimate capacity of the composite beams but also substantially reduce the maximum crack propagation width during the service stage. This demonstrates that the physical response of the dataset is reasonable, possessing excellent mechanical monotonicity and nonlinear mapping potential.

Table 6 Parametric numerical simulation dataset for UHPC-ordinary concrete composite beams

Case No.	h_u (mm)	ρ_s (%)	f_{cu} (MPa)	f_c (MPa)	$\bar{\lambda}$	Ultimate capacity P_u (kN)	Maximum crack width w_{max} (mm)
1	30	1	120	30	2	145.2	0.185
2	30	1	120	40	2.8	112.4	0.224
3	30	1.6	150	30	3.6	125.8	0.152
4	30	2.2	180	50	2	285.6	0.095
5	50	1	150	30	2.8	158.3	0.133
6	50	1.6	120	50	2	254.1	0.112
7	50	2.2	180	40	3.6	215.4	0.076
8	50	2.8	150	50	2.8	290.2	0.061
9	70	1	180	40	3.6	165.7	0.098
10	70	1.6	120	30	2.8	210.5	0.095
11	70	2.2	150	50	2	378.3	0.058
12	70	2.8	180	30	2.8	352.4	0.044
13	90	1.6	180	30	2	345.1	0.063
14	90	2.2	120	50	3.6	312.8	0.055
15	90	2.8	150	40	2.8	412.9	0.035

3.2 Parameter Sensitivity Analysis of Flexural Capacity for Composite Beams

Based on 420 groups of effective finite element simulation results, the single and coupling influence laws of design variables, such as the UHPC layer thickness (h_u), longitudinal tensile reinforcement ratio (ρ_s), ordinary concrete compressive strength (f_c), and shear span-to-depth ratio ($\bar{\lambda}$), on the ultimate flexural capacity (P_u) were systematically analyzed in this section, and their micro-mechanical mechanisms were elucidated.

3.2.1 Influence of UHPC Layer Thickness on Flexural Capacity

Under different ordinary concrete strengths, the evolution curves of the ultimate flexural capacity P_u of the composite beams with the UHPC layer thickness h_u are shown in **Fig. 3** (controlling $\rho_s = 1.6\%$, $\bar{\lambda} = 2.8$, and $f_{cu} = 150$ MPa).

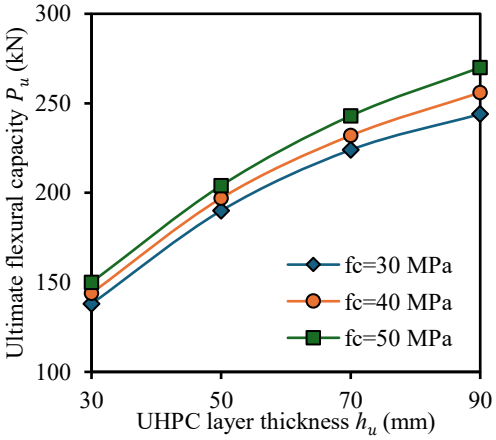

Fig. 3 Evolution curves of ultimate flexural capacity of composite beams with UHPC layer thickness under different ordinary concrete strengths ($\rho_s = 1.6\%$, $f_{cu} = 150$ MPa, and $\bar{\lambda} = 2.8$)

As can be seen from Fig. 3-1, the ultimate load-carrying capacity is significantly positively correlated with the UHPC layer thickness. When h_u increases from 30 mm to 90 mm, the overall increment in load-carrying capacity reaches 48.2% to 56.5%. The underlying mechanical mechanisms are twofold: on the one hand, an increase in h_u directly expands the proportion of the high-strength and high-ductility UHPC material in the tensile zone of the cross-section, which allows the bridging and crack mitigation contribution of the internal steel fibers to be fully exerted; on the other hand, from the perspective of cross-sectional equilibrium, an increase in h_u causes the cross-sectional neutral axis to shift downward significantly in the late stage of loading. This not only promotes earlier and more sufficient yielding of the tensile longitudinal reinforcements but also increases the lever arm of internal forces (internal force couple arm) and delays the evolution of crushing damage in the ordinary concrete within the compression zone. However, when h_u exceeds 70 mm, the marginal improvement effect on the load-carrying capacity decreases slightly. The primary reason is that an excessively thick UHPC layer triggers an excessive downward shift of the neutral axis, leading to the phenomenon where the strength utilization rate of the ordinary concrete in the compression zone cannot reach its limit, and the failure mode begins to transition toward over-reinforced characteristics.

3.2.2 Coupling Effects of Longitudinal Reinforcement Ratio and Material Strength

The three-dimensional response surface showing the two-parameter coupling effects of the longitudinal reinforcement ratio ρ_s and the ordinary concrete compressive strength f_c on the ultimate capacity P_u is presented in **Fig. 4** (controlling $h_u = 50$ mm, $f_{cu} = 150$ MPa, and $\bar{\lambda} = 2.8$).

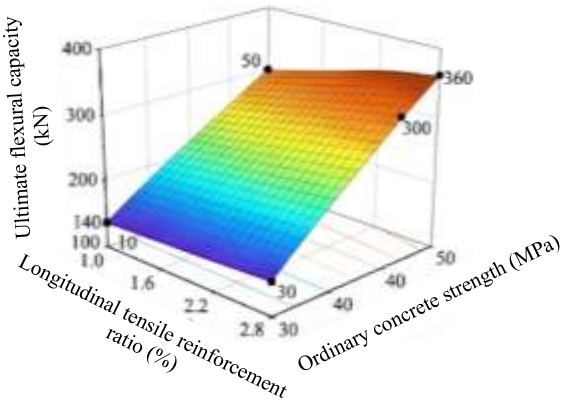

Fig. 4 Response surface showing the two-parameter coupling effects of longitudinal tensile reinforcement ratio and ordinary concrete strength on the ultimate flexural capacity P_u ($h_u =$ 50 mm, $f_{cu} = 150$ MPa, and $\bar{\lambda} = 2.8$)

As can be observed from the response surface, a strong linear positive correlation is exhibited between the longitudinal reinforcement ratio ρ_s and the load-carrying capacity P_u. Under the condition of $h_u = 50$ mm, when the reinforcement ratio is increased from 1.0% to 2.8%, a doubled growth in the ultimate capacity is achieved. This is attributed to the excellent bond performance between the steel bars and the surrounding UHPC, whereby the increase in the reinforcement ratio directly and linearly enhances the longitudinal tensile force contribution in the tensile zone.

In contrast, the enhancement effect of the ordinary concrete strength f_c on the load-carrying capacity is relatively moderate, and a significant coupling and synergistic effect with the reinforcement ratio is demonstrated. In the low reinforcement ratio state ($\rho_s = 1.0\%$), increasing f_c only causes the capacity to rise slightly by approximately 5% to 8%. At this stage, the cross-sectional failure is completely dominated by the tensile steel reinforcement strength, and a redundancy exists in the strength of the conventional concrete in the compression zone. However, in the high reinforcement ratio state ($\rho_s = 2.8\%$), the enhancement amplitude of the load-carrying capacity by increasing f_c jumps to 18.4%. Under this condition, the total tensile force in the tensile zone is extremely large, which forces the ordinary concrete in the compression zone to provide a matching compressive force. Consequently, the strength of the compression zone concrete becomes the bottleneck restricting the further growth of the load-carrying capacity. Once f_c is increased, the crushing damage of the concrete in the compression zone is delayed, and the flexural potential of the structure can be thoroughly released. Therefore, the mechanical equivalence between the tensile reinforcement characteristics and the compressive concrete strength must be maintained in the design of composite beams.

3.2.3 Macro Control of Shear Span-to-Depth Ratio on Flexural Capacity Characteristics

Under different reinforcement ratios, the degradation paths of the ultimate capacity P_u with an increase in the shear span-to-depth ratio $\bar{\lambda}$ are presented in **Fig. 5** (controlling $h_u = 50$ mm, $f_{cu} = 150$ MPa, and $f_c = 40$ MPa).

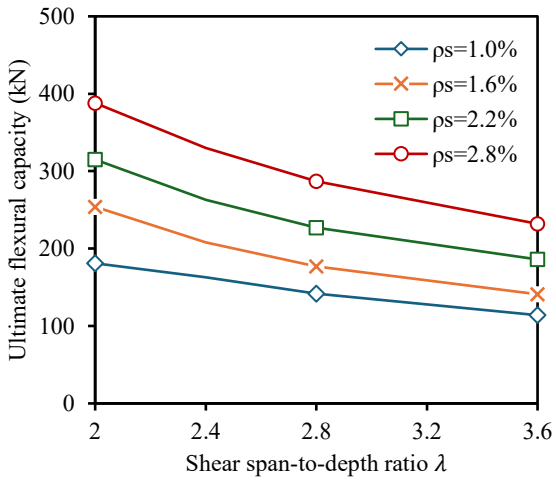

Fig. 5 Degradation paths of ultimate capacity of composite beams with shear span-to-depth ratio under different reinforcement ratios ($h_u = 50$ mm, $f_{cu} = 150$ MPa, and $f_c = 40$ MPa)

As can be analyzed from Fig. 3-3, an obvious nonlinear inverse relationship is exhibited between the ultimate capacity P_u and the shear span-to-depth ratio $\bar{\lambda}$. When the shear span-to-depth ratio increases from 2.0 to 3.6, the ultimate capacity decreases sharply, with a reduction generally ranging between 35% and 45%. This phenomenon stems from the redistribution of the flexural-shear stress flow inside the beam body. When the shear span-to-depth ratio is small ($\bar{\lambda} = 2.0$), the composite beam is in a strong flexural-shear state, and a significant arch action force transmission mechanism can be formed inside the structure. The load is directly transmitted to the supports through the concrete in the compression zone, which reduces the local tensile force demand on the longitudinal main reinforcements, and the interlaminar shear slip constraint is extremely strong, thereby exhibiting an extremely high ultimate capacity. As the shear span-to-depth ratio increases to 3.6, the arch action mechanism fails, and the beam body completely transitions to a beam action flexural force transmission mechanism. The mid-span sectional deflection increases rapidly, and the bending moment becomes the absolute factor dominating the structural failure, leading to a significant attenuation of the load-carrying capacity.

3.3 Parameter Sensitivity Analysis of Crack Width for Composite Beams

Based on the maximum physical crack width (w_{max}) data under the serviceability load ($0.6P_u$) extracted from 420 groups of finite element simulations, the influence laws of the UHPC layer thickness (h_u), longitudinal tensile reinforcement ratio (ρ_s), and shear span-to-depth ratio ($\bar{\lambda}$) on the crack width were systematically investigated in this section, and their micro-crack mitigation mechanisms were elucidated.

3.3.1 Mitigation Effect and Bridging Mechanism of UHPC Layer Thickness on Crack Propagation

Under different longitudinal reinforcement ratios, the variation curves of the maximum crack width w_{max} in the mid-span tensile zone of the composite beams with the UHPC layer thickness h_u are shown in **Fig. 6** (controlling $f_{cu} = 150$ MPa, $f_c = 40$ MPa, and $\bar{\lambda} = 2.8$).

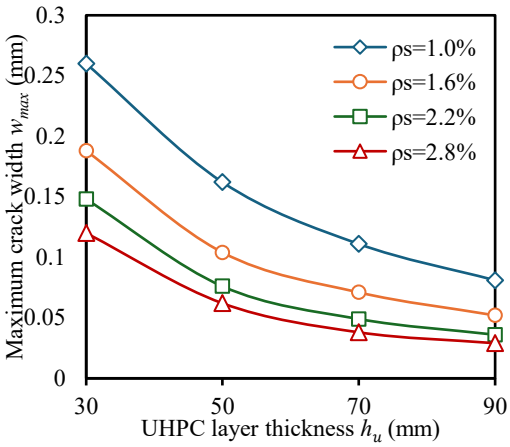

Fig. 6 Evolution curves of maximum crack width of composite beams with UHPC layer thickness under different reinforcement ratios ($f_{cu} = 150$ MPa, $f_c = 40$ MPa, and $\bar{\lambda} = 2.8$)

As can be observed from Fig. 3-4, the maximum crack width during the service stage can be significantly restricted by increasing the UHPC layer thickness. When h_u increases from 30 mm to 90 mm, an exponential attenuation is exhibited by the maximum mid-span primary crack width w_{max}, with an average reduction ranging from 60.5% to 72.1%. Under the condition of $h_u =$ 30 mm, the UHPC layer in the tensile zone is thin. After cracking, pulling out, slipping, or even snapping of a small number of steel fibers occurs rapidly, leading to a complete transfer of the stress at the cracked section to the longitudinal steel reinforcements. Consequently, the primary crack extends upward rapidly, and the width generally exceeds 0.15 mm. When h_u is increased to more than 70 mm, the maximum crack width is strictly controlled below 0.08 mm. The underlying mechanical essence is twofold: on the one hand, a thicker UHPC layer provides a fiber bridging zone with a larger cross-sectional area along the crack path. The continuous fiber bridging stress restricts the localized concentration of tensile plastic strain at the primary cracking surface, which transforms the beam bottom failure from a traditional single wide and deep primary crack mode to multi-diffuse, fine, and dense micro-crack characteristics. On the other hand, thickening the UHPC layer enhances the equivalent composite stiffness in the tensile zone and delays the degradation of bond-slip between the steel bars and the matrix, thereby suppressing the opening of macroscopic primary cracks.

3.3.2 Synergistic Effects of UHPC Layer Thickness and Longitudinal Reinforcement Ratio on Crack Control

The three-dimensional response surfaces showing the two-parameter coupling effects of the UHPC layer thickness h_u and the longitudinal reinforcement ratio ρ_s on the maximum crack width w_{max} under different shear span-to-depth ratios are presented in **Fig. 7** (controlling $f_{cu} =$ 150 MPa and $f_c = 40$ MPa).

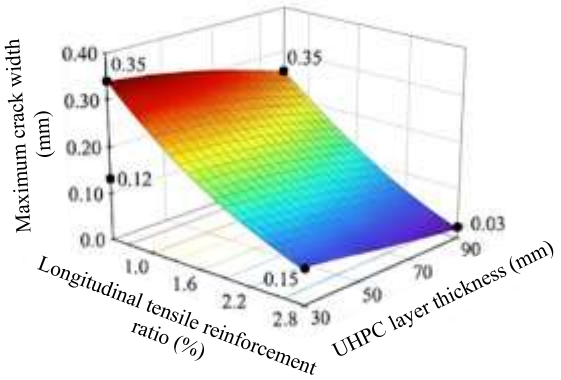

Fig. 7 Response surface showing the two-parameter coupling effects of UHPC layer thickness and longitudinal reinforcement ratio on the maximum crack width w_{max} ($f_{cu} = 150$ MPa, $f_c = 40$ MPa, and $\bar{\lambda} = 2.8$)

As can be observed from the response surface, a strong synergistic crack mitigation effect is exhibited between the reinforcement ratio ρ_s and the UHPC thickness h_u. In the low reinforcement ratio state ($\rho_s = 1.0\%$), although the crack width can be reduced by solely increasing h_u, localized cracks are still prone to sudden opening under a load of $0.6P_u$ due to the insufficient macroscopic restraining tensile force provided by the steel bars. Conversely, when the reinforcement ratio is increased to 2.8%, a perfect complementarity is formed between the high axial stiffness of the steel bars and the steel fiber bridging force of the UHPC matrix. The deflection deformation and average tensile strain of the beam body are restricted macroscopically by the steel bars, whereas the outward extension of shear-slip cracks on the steel bar surface is hindered microscopically by the UHPC. A near-micro-crack state ($w_{max} < 0.05$ mm) under the serviceability load is achieved in the composite beams with high reinforcement and a thick UHPC layer through this dual restraint. The tensile strain in the mid-span tensile zone presents a wide range of uniform distribution, whereby the phenomenon of severe strain accumulation at a single crack is effectively avoided.

3.3.3 Macro Mechanism of Shear Span-to-Depth Ratio on Crack Distribution and Evolution

Under different UHPC thicknesses, the development paths of the maximum crack width w_{max} with an increase in the shear span-to-depth ratio $\bar{\lambda}$ are shown in **Fig. 8** (controlling $\rho_s = 1.6\%$, $f_{cu} = 150$ MPa, and $f_c = 40$ MPa).

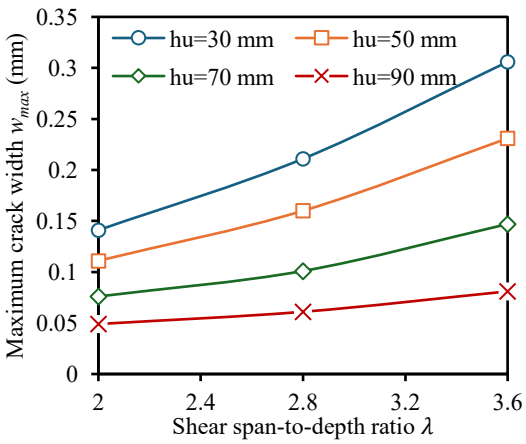

Fig. 8 Variation curves of maximum crack width of composite beams with shear span-to-depth ratio under different UHPC thicknesses ($\rho_s = 1.6\%$, $f_{cu} = 150$ MPa, and $f_c = 40$ MPa)

As can be observed from Fig. 3-6, under the same load level ratio ($0.6P_u$), an approximately linear increase is exhibited by the maximum crack width w_{max} with the increase in the shear span-to-depth ratio $\bar{\lambda}$. When the shear span-to-depth ratio $\bar{\lambda} = 2.0$, the composite beam is in a strong flexural-shear state, the principal tensile stress points diagonally toward the supports, and the cracks are primarily controlled by the inclined cracks in the flexural-shear segment. At this stage, because strong shear extrusion and friction exist at the interface, the projected width of the inclined cracks in the longitudinal section direction is relatively narrow. When the shear span-to-depth ratio increases to 3.6, the structure completely enters the pure flexural control zone, the principal tensile stress is almost parallel to the axis of the tensile longitudinal reinforcements, and the primary cracks manifest as vertical flexural primary cracks. Due to the rapid and severe sudden change in the cross-sectional curvature at the mid-span caused by the lengthened shear span, the strain hardening capacity of the UHPC in the tensile zone is rapidly exhausted locally. Consequently, large-scale pulling out of steel fibers at the primary crack is triggered, leading to the accelerated formation and upward extension of wide and deep cracks in the pure flexural segment. Therefore, the crack control capability of the UHPC layer within the pure flexural segment should be targeted and strengthened in the design of composite beams with large shear span-to-depth ratios.

4 Machine Learning-Based Prediction of Load-Carrying Capacity and Crack Width

4.1 Machine Learning Data Preprocessing and Algorithm Selection

When establishing a high-precision prediction model for the flexural performance of UHPC-concrete composite beams, the algorithm selection and preprocessing strategies are the keys to determining the generalization capability of the model. Because the dimension of the independent variables is moderate (5 features) and the non-linearity of the dependent variables is extremely strong (especially the crack width w_{max}), selecting feature engineering methods and differentiated algorithm architectures suitable for tabular data can fundamentally circumvent the risks of overfitting or training underfitting.

4.1.1 Feature Engineering and Normalization of Data

A total of 420 validated simulation samples were contained in this database. Significant differences exist in the physical dimensions and numerical ranges of the input features ($h_u, \rho_s, f_{cu}, f_c, \bar{\lambda}$). To prevent features with larger absolute scales from dominating model gradient descent, data standardization was performed. To prevent data leakage during model evaluation, the dataset was first split into training and testing sets. The Min-Max normalization mapping parameters were computed exclusively from the training set and subsequently applied to normalize both the training and independent testing sets into the range of $[0,1]$:

$$x^* = \frac{x - x_{\min,\text{train}}}{x_{\max,\text{train}} - x_{\min,\text{train}}} \tag{4}$$

where x is the raw feature value; $x_{\min,\text{train}}$ and $x_{\max,\text{train}}$ are the minimum and maximum values of the feature in the training subset, respectively.

To visually demonstrate the synergistic correlations among features and exclude collinearity issues, the heatmap of the Pearson correlation coefficient matrix between the five input features and the two target responses (ultimate capacity P_u, maximum crack width w_{max}) in the dataset was plotted in **Fig. 9**.

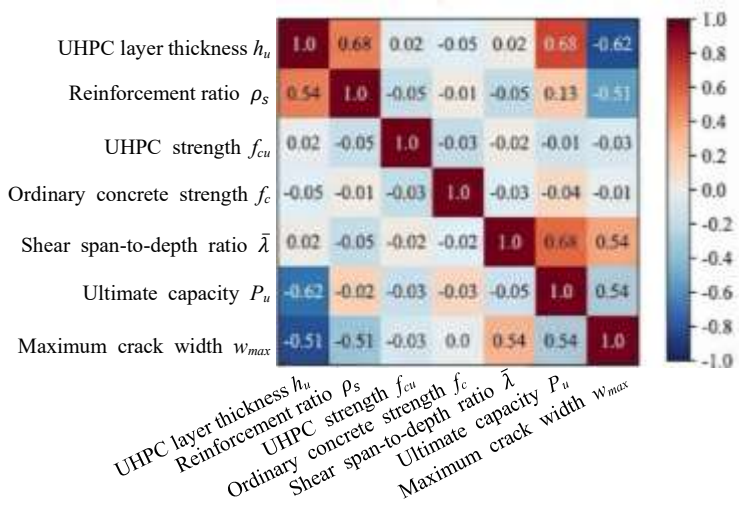

Fig. 9 Heatmap of Pearson correlation matrix between input design features and output target responses of composite beams

As can be analyzed from **Fig. 9**, a strong positive correlation is exhibited between P_u and the reinforcement ratio ρ_s ($r = 0.68$) as well as the UHPC thickness h_u ($r = 0.54$), which conforms to the physical law that the flexural capacity is dominated by the materials in the tensile and compression zones. Conversely, a significant negative correlation is exhibited between w_{max} and h_u ($r = -0.62$) as well as ρ_s ($r = -0.51$), which verifies the crack control dividend of thickening the UHPC layer and increasing the reinforcement ratio. The correlation coefficients among the five input features are all close to 0, proving that the independent variables are mutually independent and the interference of multicollinearity is eliminated.

4.1.2 Architecture Design and Selection of Prediction Algorithms

Aiming at the multi-objective prediction of load-carrying capacity and crack width, three representative algorithm architectures were constructed and horizontally compared in this study:
Extreme Gradient Boosting (XGBoost): An ensemble learning method based on the forward distribution algorithm, where the true response is iteratively approximated by multiple classification and regression trees (CARTs). A second-order Taylor expansion and a regularization penalty term are introduced into the loss function, which possesses a strong capability to suppress overfitting and excels at capturing local extreme values and strong nonlinear boundaries.

Random Forest (RF): An ensemble algorithm based on the Bagging framework, where multiple decision trees are constructed through bootstrap resampling. The sensitivity of the model to noise is reduced through dual random sampling of both samples and features, and a stable generalization performance is achieved.

Artificial Neural Network (ANN): A four-layer feedforward backpropagation (BP) neural network was constructed, consisting of one input layer (5 nodes), two hidden layers (with 16 and 8 nodes, respectively), and one output layer. The Rectified Linear Unit (ReLU) activation function was implemented in the hidden layers to prevent gradient vanishing issues, and weights were optimized using the Adam optimizer with a learning rate of 0.001.

4.1.3 Model Training and Hyperparameter Tuning Strategy

The 420 groups of effective dataset were randomly partitioned into a training set (336 groups) and an independent testing set (84 groups) according to a ratio of 8:2 in this study.

To avoid the contingency of a single partition, a 5-fold cross-validation mechanism was

introduced within the training set during model training. Meanwhile, the grid search algorithm was adopted to optimize the core hyperparameters. Through the optimization, it was determined that for the XGBoost model, the maximum tree depth max_depth is 5, the learning rate learning_rate is 0.05, and the number of base estimators n_estimators is 250. For the ANN model, the learning rate was set to 0.001, and the number of training epochs was fixed at 1000. These settings were employed to ensure that each algorithm participated in the accuracy comparison in its optimal state.

4.2 Prediction Results of Flexural Capacity and Comparison among Different Models

The prediction performance of three algorithms, including XGBoost, Random Forest (RF), and Artificial Neural Network (ANN), on the ultimate flexural capacity (P_u) was comprehensively evaluated in this section. The generalization capability of each model was evaluated using the independent testing set (84 groups of independent samples), and the sources of errors were deeply analyzed from the two dimensions of the algorithm mapping mechanism and the stiffness mutation behavior of composite beams.

4.2.1 Quantitative Evaluation of Prediction Accuracy and Multi-Indicator Comparison

Three statistical indicators, including the coefficient of determination (R^2), root mean square error (RMSE), and mean absolute error (MAE), were introduced to quantitatively evaluate the prediction accuracy of each algorithm. The performances of the three models on the training set and the independent testing set are summarized in **Table 7**.

Table 7 Comparison of prediction performance indicators of ultimate flexural capacity P_u for different machine learning models

Prediction model	Coefficient of determination R^2 of training set	Coefficient of determination R^2 of testing set	RMSE of training set (kN)	RMSE of testing set (kN)	MAE of training set (kN)	MAE of testing set (kN)
XGBoost	0.994	0.988	4.12	6.45	3.02	4.82
Random Forest (RF)	0.989	0.978	5.68	8.24	4.15	6.18
ANN	0.978	0.965	7.92	10.35	5.84	8.12

As can be observed from **Table 7**, the coefficients of determination (R^2) of the three machine learning algorithms on the independent testing set all exceed 0.95, which proves the effectiveness of the data-driven models in handling the fast prediction task of the flexural capacity of dual-material composite structures.

Among them, the highest R^2 value of 0.988 on the testing set is achieved by the XGBoost model, with its testing set RMSE and MAE as low as 6.45 kN and 4.82 kN, respectively. Compared with the RF model, the testing set RMSE of the XGBoost model is reduced by 21.7%. Compared with the classic ANN model architecture, its testing set RMSE is substantially decreased by 37.7%. The statistical indicators demonstrate that the gradient-boosting decision tree architecture exhibits a more superior residual approximation capability than the Bagging architecture (RF) and the multilayer perceptron (ANN) when processing such tabular data with continuous nonlinear features.

4.2.2 Fitting Distribution Laws of Predicted Values and True Values

To visually present the predicted scatter distribution of each algorithm on the testing set, the comparison scatter plots between the predicted values of the three models and the true finite element values ($P_{u,\mathrm{FEA}}$) are shown in **Fig. 10**. The dashed line in the figure represents the $y = x$ ideal

prediction line, and the shaded regions represent the error envelope boundaries of $\pm 5\%$ and $\pm 10\%$, respectively.

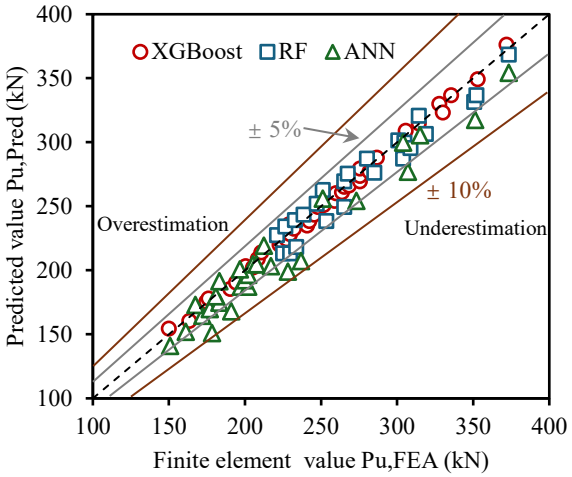

Fig. 10 Comparison scatter plots between predicted values of ultimate flexural capacity and true finite element values on the testing set for three machine learning models

As can be observed from the spatial arrangement of the scatter points in **Fig. 10**, the testing set sample points of the XGBoost model are almost completely and tightly clustered on both sides of the $y = x$ ideal line, and no outliers exceeding the $\pm 10\%$ error envelope line exist within the full range (100 kN to 450 kN). The scatter points of the Random Forest (RF) model are relatively concentrated in the mid-range, but a slight discreteness is exhibited in the high load-carrying capacity range (greater than 350 kN). The prediction points of the Artificial Neural Network (ANN) model exhibit the highest discreteness across the full range, and a relatively obvious systematic underestimation phenomenon occurs at the boundary nodes of the low range (less than 150 kN) and the high range (greater than 380 kN).

The probability density function (PDF) curves of the residuals (Residual $= P_{u,\text{pred}} - P_{u,\text{FEA}}$) corresponding to the three prediction models are plotted in **Fig. 11**. The residual distribution of the XGBoost model exhibits extremely high symmetry, and the residual center is highly aggregated at the 0 kN baseline. The full width at half maximum (FWHM) of its curve is significantly narrower than those of the other two models. Conversely, the residual PDF curve of the ANN model is broader as a whole, and a slight negative skewness exists in the distribution center, which statistically confirms its tendency toward conservative underestimation in the full-range prediction.

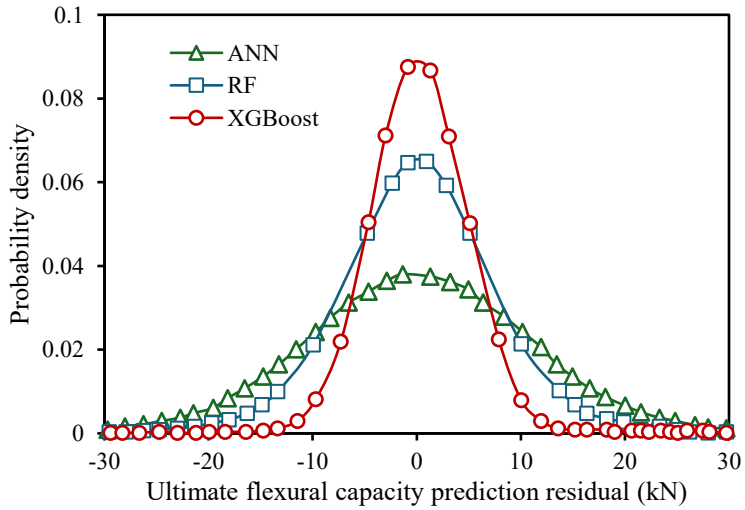

Fig. 11 Probability density distribution curves of prediction residuals for ultimate flexural capacity of three machine learning models

4.3 Prediction Results of Crack Width and Comparison among Different Models

Under the serviceability limit state (SLS) of structures, the maximum crack width (w_{max}) on the tensile side is a core indicator for evaluating the durability of UHPC-concrete composite beams. Compared with the ultimate capacity P_u, the prediction of w_{max} under the serviceability load ($0.6P_u$) possesses higher strong non-linearity and discreteness. This is primarily because cracking depends not only on macroscopic internal forces but is also governed by accidental physical mechanisms, such as the bridging effect of the spatial random distribution of steel fibers inside the UHPC and micro-slip degradation.

4.3.1 Quantitative Evaluation of Crack Prediction Accuracy and Multidimensional Indicator Comparison

Aiming at the nonlinear characteristics of the maximum crack width w_{max}, the coefficient of determination (R^2), root mean square error (RMSE), and mean absolute error (MAE) were adopted in this study to evaluate the prediction accuracy of the three models for w_{max}. The statistical indicators are summarized in **Table 8**.

Table 8 Comparison of prediction performance indicators of maximum crack width w_{max} for different machine learning models

Prediction model	Coefficient of determination R^2 of training set	Coefficient of determination R^2 of testing set	RMSE of training set (mm)	RMSE of testing set (mm)	MAE of training set (mm)	MAE of testing set (mm)
XGBoost	0.985	0.968	0.008	0.012	0.006	0.009
Random Forest (RF)	0.964	0.932	0.013	0.018	0.009	0.013
ANN	0.941	0.895	0.017	0.024	0.012	0.018

By comparing **Table 7** and **Table 8**, it can be found that due to the high discreteness of the crack evolution task, the accuracy of all algorithms on the testing set decreases compared with the load-carrying capacity prediction. The testing set R^2 of the traditional ANN model drops to 0.895, whereby an obvious fitting bottleneck is exhibited. In contrast, the optimal performance is still maintained by the XGBoost model, with its testing set R^2 reaching 0.968 and the MAE being only 0.009 mm. Compared with the RF and ANN models, the testing set MAE of the XGBoost model is reduced by 30.8% and 50.0%, respectively, demonstrating an excellent error control capability.

4.3.2 Prediction Deviation Distribution Laws and Comparison of Error Limits

To visually investigate the fitting quality of the three algorithms for the crack width, the comparison scatter plots between the predicted values of the three models and the true finite element values on the testing set are shown in **Fig. 12** (including double error envelopes of $\pm 10\%$ and $\pm 20\%$). The sample points of the XGBoost model are closely distributed around the $y = x$ equality line within the full range (0.03 mm to 0.30 mm), and high accuracy can still be maintained especially in the micro-crack zone where w_{max} is less than 0.08 mm. Obvious scattering is exhibited by the scatter points of the Random Forest (RF) model in the two extreme ranges. In contrast, spindle-shaped scattering characteristics are presented by the ANN model, where overestimation is commonly observed in the micro-crack zone, and systematic underestimation occurs in the large crack zone (greater than 0.25 mm).

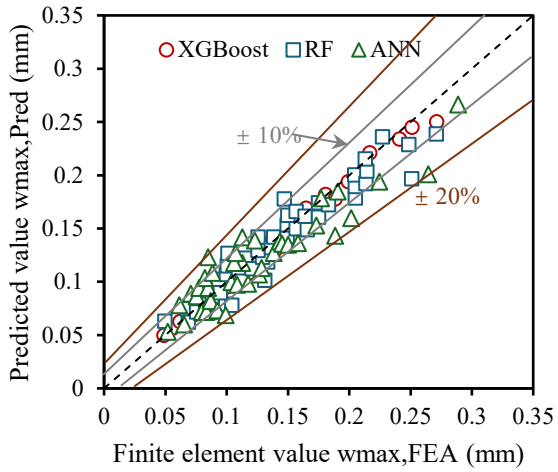

Fig. 12 Comparison scatter plots between predicted values of maximum crack width and true finite element values on the testing set for three machine learning models

To deeply quantify the error concentration degree of each algorithm, the cumulative probability distribution curves of absolute error on the testing set for the three prediction models are displayed in **Fig. 13**. The reliability of the models under a given error threshold can be visually reflected by this figure.

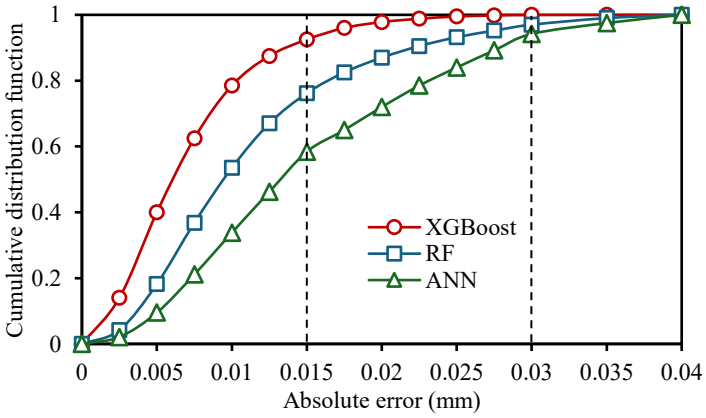

Fig. 13 Cumulative distribution function (CDF) curves of absolute error for predicting maximum crack width by three machine learning models

As can be observed from **Fig. 13**, when the allowable engineering absolute error is restricted to 0.015 mm, 92.5% of the samples in the XGBoost model can meet the accuracy requirements, whereas only 76.2% and 58.4% are satisfied by the RF and ANN models, respectively. When the error limit is relaxed to 0.030 mm, 100% sample coverage has been achieved by the XGBoost model, which again confirms the reliability of its prediction results.

5 Discussion

5.1 Comparative Analysis with Traditional Code Formulas

The optimal XGBoost prediction model is horizontally compared with the Chinese code (GB 50010-2010), the American code (ACI 318-19), and the European code (Eurocode 2) in this section. Due to the lack of special calculation formulas for UHPC-concrete composite beams in the current codes, the traditional reinforced concrete (RC) flexural and crack control calculation models were extended according to the general practice of the industry, and the tensile contribution of the UHPC in the tensile zone was introduced. These adjustments were employed to quantitatively evaluate the

limitations of traditional semi-empirical code formulas when dealing with this new type of composite structure.

5.1.1 Rational Extension and Equivalent Transformation of Code Calculation Formulas

In terms of the modification of the ultimate flexural capacity P_u, the plane section assumption and the equivalent rectangular stress diagram are based upon by all codes, and the equivalent tensile contribution of the UHPC layer was included in the ultimate equilibrium equations in this study. Among them, the design value of the axial tensile strength of UHPC $f_{t,u}$ is introduced in the modified GB 50010 model (taking the steel fiber bridging reduction coefficient $\eta_b = 0.4$), and the calculation formula for the ultimate flexural capacity of the equivalent cross-section is expressed as $M_{u,\mathrm{GB}} = f_c bx(h_0 - x/2) + f_y A_s(h_0 - a_s') + \eta_b f_{t,u} b h_u(h - h_u/2 - x/2)$. The equivalent rectangular stress block coefficient β_1 is adopted in the modified ACI 318 model, and the tensile softening reduction factor of fiber-reinforced concrete is introduced according to the ACI-544 report to equivalent the UHPC tensile strength to a uniformly distributed tensile stress. The bilinear tensile constitutive relationship is utilized in the modified Eurocode 2 model to integrate the stress distribution of the UHPC cross-section in the tensile zone.

In terms of the calculation model for the maximum crack width w_{max}, the formula $w_{max} = \alpha_{cr}\psi\frac{\sigma_s}{E_s}\left(1.9c + 0.08\frac{d_{eq}}{\rho_{te}}\right)$ is adopted in the GB 50010 model, where ψ is the non-uniformity coefficient of reinforcement strain between cracks. Because the fiber crack mitigation effect is not included, the tensile hardening characteristic of UHPC cannot be accurately reflected by this formula. The formula $w_{max} = s_{r,max}(\varepsilon_{sm} - \varepsilon_{cm})$ is adopted in the Eurocode 2 model, where $s_{r,max}$ is the maximum crack spacing, and $\varepsilon_{sm} - \varepsilon_{cm}$ is the average strain difference between the steel reinforcements and the concrete.

5.1.2 Code Comparison for Prediction of Ultimate Flexural Capacity

The testing set (84 groups of samples) was substituted into the modified code formulas and the XGBoost model, and the statistical distributions of the prediction ratios ($P_{u,\mathrm{pred}}/P_{u,\mathrm{FEA}}$) are shown in **Fig. 14**. The median prediction ratio of the XGBoost model is 1.002, and an extremely narrow box is presented (50% of the data are concentrated between 0.98 and 1.02), demonstrating unbiased and highly stable prediction characteristics. The median prediction ratio of the modified GB 50010 code is 0.854, exhibiting an obvious conservative underestimation tendency. The primary reason is that the plastic redistribution of high-strength materials is considered cautiously in the Chinese code, and the value of the equivalent tensile reduction coefficient ($\eta_b = 0.4$) is on the safe side. The prediction medians of the modified ACI 318 and Eurocode 2 codes are 0.886 and 0.912, respectively. Although the fitting means are slightly better than that of the national standard, the discreteness (box height) is significantly larger than that of the XGBoost model. Especially under the conditions of a high reinforcement ratio and a thick UHPC layer, the underestimation amplitude of both codes reaches more than 25%.

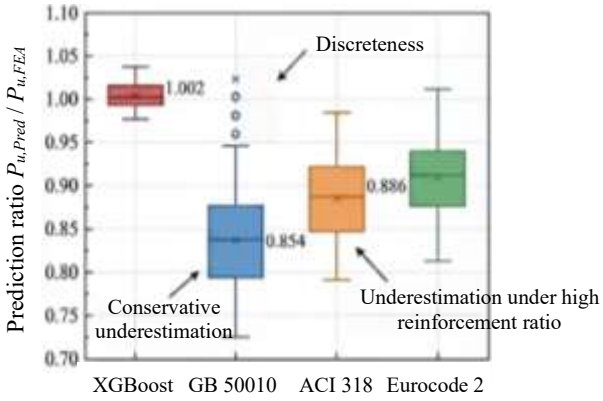

Fig. 14 Box plot comparison of prediction ratios ($P_{u,\text{pred}}/P_{u,\text{FEA}}$) for ultimate flexural capacity between XGBoost model and mainstream design codes (GB 50010, ACI 318, Eurocode 2)

5.1.3 Code Comparison for Prediction of Maximum Crack Width

The root mean square error (RMSE) distributions for predicting w_{max} by the traditional code formulas and the XGBoost model under different UHPC thicknesses are shown in **Fig. 15**. As can be analyzed from the radar chart data, the RMSE values of the traditional code formulas are significantly larger. Under all UHPC thickness conditions, the prediction errors of GB 50010, ACI 318, and Eurocode 2 all reach 3 to 8 times that of the XGBoost model. Meanwhile, the code prediction accuracy deteriorates sharply with an increase in thickness. When $h_u = 30$ mm, the prediction RMSE of GB 50010 is 0.045 mm, whereas when h_u increases to 90 mm, its RMSE soars to 0.115 mm (at this stage, the actual crack width is only around 0.035 mm, indicating an overestimation of nearly 3 times by the code formula). In contrast, the RMSE can be stably controlled within 0.015 mm under all thicknesses by the XGBoost model, demonstrating extremely strong value for practical engineering applications.

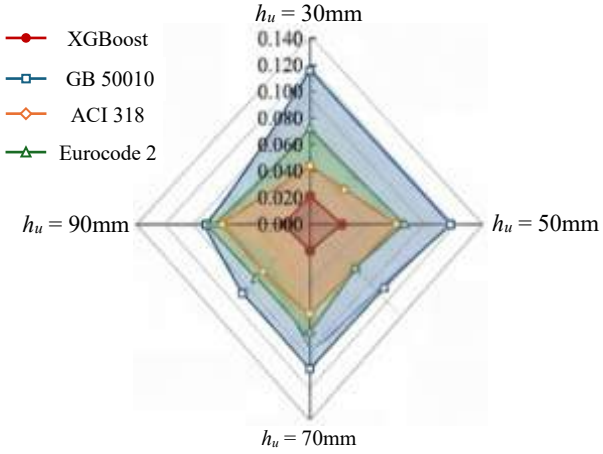

Fig. 15 Radar chart comparison of RMSE dimension for maximum crack width prediction between three code formulas and XGBoost model under different UHPC thicknesses

5.2 SHAP-Based Interpretability Analysis of Model Mechanics

Although excellent accuracy is achieved by the XGBoost model in predicting the flexural capacity and crack width, the nested splitting structure of the ensemble tree algorithm gives it a black-box characteristic. For this reason, the SHAP interpretability framework based on the cooperative solution of game theory was introduced in this section. The model prediction results were decomposed into the additive marginal contribution values (SHAP values) of each input design

feature, whereby the prediction model was parsed via a white-box approach from the dual dimensions of data science and structural mechanics.

5.2.1 Theoretical Foundation of SHAP and Additive Explanation Model

The core idea of the SHAP method stems from the Shapley value in cooperative game theory. In this prediction scenario, the five input features of the composite beams are regarded as players in the game, whereas the predicted ultimate capacity P_u or crack width w_{max} is treated as the total gain. For any sample condition i, its predicted value $g(x_i)$ can be expressed as the sum of the baseline value and the SHAP value of each feature:

$$g(x_i) = \phi_0 + \sum_{j=1}^{M} \phi_j(x_i) \tag{5}$$

where ϕ_0 is the baseline expected output value, and $\phi_j(x_i)$ is the SHAP value of the j-th feature. $\phi_j(x_i) > 0$ indicates that the predicted result is promoted by this feature (increasing the capacity or expanding the crack width), and vice versa. The absolute weight of each feature can be quantitatively evaluated by this method, and its nonlinear physical response under different value ranges can be captured.

5.2.2 Global Sorting Analysis of Feature Importance

To evaluate the absolute importance and relative contribution of each feature to the target predictions, the mean absolute SHAP value ($\bar{\phi}_j$) and normalized relative importance rate ($I_{r,j}$) across N testing samples were formulated as:

$$\bar{\phi}_j = \frac{1}{N}\sum_{i=1}^{N}\left|\phi_j(x_i)\right| \tag{6}$$

$$I_{r,j} = \frac{\bar{\phi}_j}{\sum_{k=1}^{M}\bar{\phi}_k} \times 100\% \tag{7}$$

where $\phi_j(x_i)$ represents the SHAP value of feature j for sample i; M is the total number of features ($M = 5$). The results are shown in **Fig. 16**.

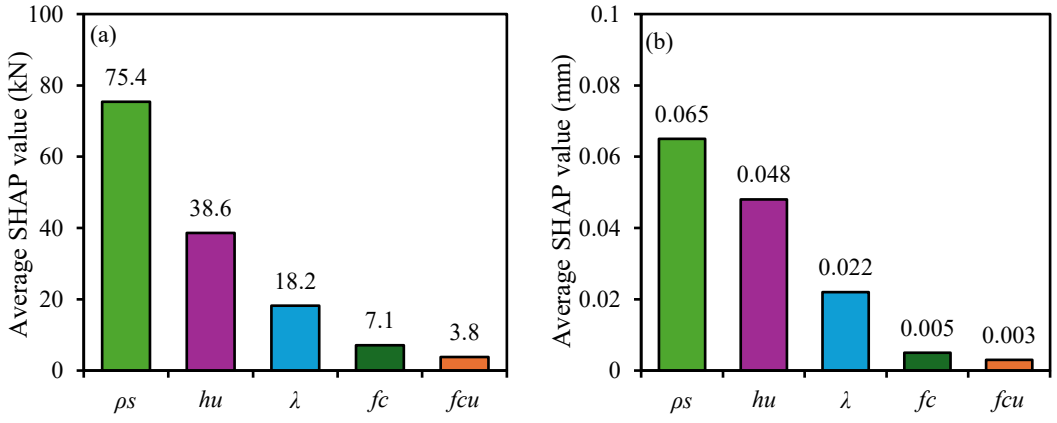

Fig. 16 Histogram of global feature importance based on average absolute SHAP values: (a) ultimate flexural capacity P_u; (b) maximum crack width w_{max}

For the ultimate flexural capacity (P_u), the mean absolute SHAP value of the longitudinal tensile reinforcement ratio (ρ_s) reaches $\bar{\phi} = 75.4$ kN ($I_r = 51.2\%$), followed by the UHPC layer thickness h_u ($\bar{\phi} = 38.6$ kN, $I_r = 26.2\%$). The cumulative relative contribution rate of these two structural features exceeds 77.4%, quantitatively establishing that ultimate failure is predominantly

governed by the mechanical properties of the tensile region.

For the maximum crack width ($w_{\max}$), the feature priority shifts dramatically toward crack-bridging constraints. The UHPC layer thickness (h_u) exhibits the highest mean absolute SHAP value of $\bar{\phi} = 0.065$ mm, yielding a dominant relative contribution rate of $I_r = 42.5\%$ (calculated via $0.065/(0.065 + 0.048 + 0.022 + 0.011 + 0.007) \times 100\%$). This is closely followed by the longitudinal reinforcement ratio ρ_s ($\bar{\phi} = 0.048$ mm, $I_r = 31.4\%$) and the shear span-to-depth ratio $\bar{\lambda}$ ($\bar{\phi} = 0.022$ mm, $I_r = 14.4\%$). This attribution confirms that serviceability crack propagation is primarily suppressed by the micro-crack mitigation capacity provided by the high-density fiber-bridging zone within thicker UHPC layers.

5.2.3 Feature Response Beehive Plots and White-Box Verification of Nonlinear Mechanical Mechanisms

The SHAP summary beehive plots of the prediction models for the ultimate capacity P_u and the maximum crack width w_{max} are shown in **Fig. 17**. The horizontal coordinate of the scatter points in the figure represents the SHAP value, and the color from blue to red represents the feature value from low to high.

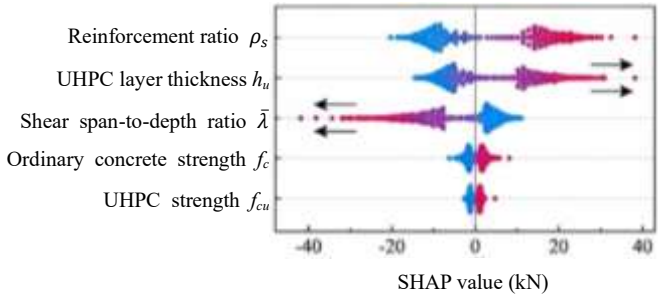

(a) SHAP summary beehive plot for ultimate flexural capacity prediction model

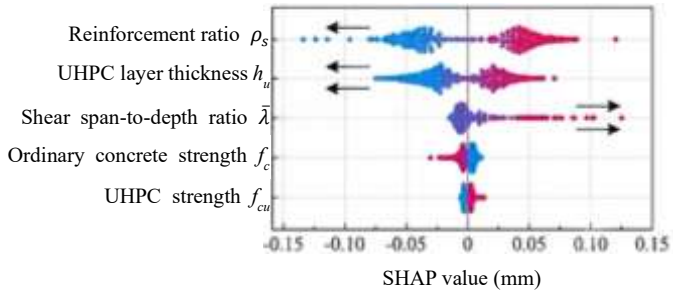

(b) SHAP summary beehive plot for maximum crack width prediction model



Fig. 17 Feature summary beehive distribution plots of the prediction models for composite beams: (a) ultimate flexural capacity P_u; (b) maximum crack width w_{max}

In the prediction of the ultimate capacity P_u, the scatter colors of the reinforcement ratio ρ_s and the UHPC thickness h_u smoothly gradient from blue to red from left to right, indicating a continuous and monotonic positive promotion effect of both features on the capacity. The high values (red points) of the shear span-to-depth ratio $\bar{\lambda}$ are significantly aggregated in the negative SHAP value zone (reaching up to -28 kN on the leftmost side). This conforms to the mechanical essence that a large shear span-to-depth ratio leads to a flattened bending moment gradient, and the failure of the arch action mechanism triggers capacity degradation. The red points of the ordinary concrete strength f_c are concentrated in the weak positive value zone close to 0, confirming the

law that redundancy exists in the strength of the ordinary concrete in the compression zone during tension-controlled failure.

In the prediction of the maximum crack width w_{max}, the high values (red points) of the UHPC thickness h_u and the reinforcement ratio ρ_s are highly clustered in the negative SHAP value zone (reaching up to -0.09 mm on the leftmost side), directly proving that strong crack control dividends can be generated by increasing the UHPC thickness and reinforcement ratio. The high shear span-to-depth ratio (red points) is widely distributed in the positive SHAP value interval. The primary reason is that an increase in the shear span-to-depth ratio aggravates the flexural deformation and the beam bottom curvature, which promotes the accelerated localized pull-out softening of steel fibers at the primary crack. The scatter points of the material strength characteristics f_{cu} and f_c are symmetrically and vertically stacked near the zero-value line, indicating that the origin of crack control lies in the toughness constraint of the tensile zone rather than the compressive strength of the matrix. The aforementioned highly consistent laws of damage mechanics are spontaneously emerged from the XGBoost model without inputting mechanical equations, which powerfully demonstrates the correctness of its physical mechanism and its generalization reliability.

6 Conclusions

Based on high-fidelity nonlinear finite element simulations and interpretable machine learning, multi-objective prediction and crack control mechanism analysis were carried out in this study for the ultimate capacity (P_u) and the maximum crack width (w_{max}) of UHPC-concrete composite beams. The main conclusions are summarized as follows:

Construction of a high-fidelity database with large samples: Based on a three-dimensional nonlinear finite element model calibrated by physical tests, a high-quality numerical test database containing 420 groups of full-factorial working conditions was successfully constructed through Python secondary development. The mesh convergence analysis demonstrates that the baseline element size of 20 mm can strictly control the prediction errors of load-carrying capacity and bending stiffness within 2.35% while balancing computational efficiency, which overcomes the generalization problem of small samples caused by the scarcity of physical tests for this new type of composite structure from the source.

Multi-objective adaptive high-precision prediction: Among the evaluated data-driven architectures, the XGBoost model achieved optimal predictive performance on the independent testing set. The root mean square errors (RMSE) for P_u and $w_{\max}$ were constrained to 6.45 kN and 0.012 mm, respectively (with R^2 values exceeding 0.968). Multi-dimensional comparative evaluation quantitatively deconstructed the excessive conservatism and systematic distortion of mainstream design codes (GB 50010, ACI 318, Eurocode 2) within small-crack micro-cracking regions.

White-box verification of algorithmic physical mechanisms: The SHAP interpretability framework successfully unboxed the ensemble machine learning model. Global feature importance attribution revealed that the UHPC layer thickness (h_u) plays a primary role in serviceability crack control, yielding a relative contribution rate of up to 42.5%. The feature interaction response surfaces spontaneously captured physical mechanisms aligned with classical concrete damage mechanics—quantifying that increasing h_u from 30 mm to 90 mm induces an exponential decay in beam-bottom crack width (average reduction of 60.5%–72.1%).

7 References

[1] Al-Osta, M. A., Isa, M. N., Baluch, M. H., & Rahman, M. K. (2017). Flexural behavior of reinforced concrete beams strengthened with ultra-high performance fiber reinforced concrete. Construction and Building Materials, 134, 279-296.

[2] Anish, V., & Logeshwari, J. (2024). A review on ultra high-performance fibre-reinforced concrete with nanomaterials and its applications. Journal of Engineering and Applied Science, 71(1), 25.

[3] Wang, D., Shi, C., Wu, Z., Xiao, J., Huang, Z., & Fang, Z. (2015). A review on ultra high performance concrete: Part II. Hydration, microstructure and properties. Construction and Building Materials, 96, 368-377.

[4] Farahzadi, L., Nia, S. B., Shafei, B., & Kioumarsi, M. (2025). Sustainability assessment of ultra-high performance concrete made with various supplementary cementitious materials. Cleaner Materials, 15, 100301.

[5] Liu, J., Zhang, G., & Guo, D. S. (2026). Experimental study on section optimization and flexural behavior of UHPC-NC composite beams. International Journal of Structural Integrity, 17(1), 77-101.

[6] Long, J., Xiong, Y., Fu, H., & Tian, L. (2025). Flexural performance of UHPC-NC composite beams under different interface treatments: experimental, numerical analysis, and design assessment. Journal of Building Engineering, 113566.

[7] Xing, L. L., Mei, K. H., Guo, Y. P., Yang, Z. H., & Sun, S. J. (2025). Flexural performances of steel-basalt fiber composite bars-reinforced ultra-high performance concrete-normal concrete layered beams: Experimental, theoretical and numerical investigation. Construction and Building Materials, 487, 142086.

[8] Lin, P., Yan, W., Zhao, H., & Ma, J. (2023). Theoretical and experimental investigation on the flexural behaviour of prestressed NC-UHPC composite beams. Materials, 16(2), 879.

[9] Zhou, S., Zhang, H., Li, H., Zhang, J., Xu, H., Li, J., & Chen, Q. (2026). Mechanical behavior, sulfate-resistance, and economic assessment of biochar-enhanced ultra-high-performance concrete. Construction and Building Materials, 523, 146273.

[10] Kang, J., Wang, D., Cui, C., He, F., Shi, J., & Shen, J. (2025). Experimental and analytical research on the flexural behavior of dismountable prefabricated composite beams with wet joint under hogging moment. Construction and Building Materials, 495, 143588.

[11] Ahmed, F. B., Biswas, R. K., Sen, D., & Tasnim, S. (2024). Flexural and shear strengthening of reinforced-concrete beams with ultra-high-performance concrete (UHPC). Construction Materials, 4(2), 468-492.

[12] Zhang, Z., Ashour, A., Ge, W., Sushant, S., Yao, S., Luo, L., ... & Li, S. (2024). Experimental and numerical study on flexural performance of ultra-high performance concrete frame beams reinforced with steel-FRP composite bars. Engineering Structures, 321, 119012.

[13] Turker, K., & Torun, I. B. (2020). Flexural performance of highly reinforced composite beams with ultra-high performance fiber reinforced concrete layer. Engineering Structures, 219, 110722.

[14] Cai, T., He, Z. Q., & Li, W. (2025). Experimental and Theoretical Study on the Flexural Behavior of NC-UHPC Composite Beams with Embedded Thin UHPC Layers. Case Studies in Construction Materials, e05725.

[15] Zhang, Y., Zhu, P., Wang, X., & Wu, J. (2020). Shear properties of the interface between ultra-

high performance concrete and normal strength concrete. Construction and Building Materials, 248, 118455.

[16] Chen, L., Yan, J., Wu, Z., Yang, D., Li, J., & Xiang, N. (2023, September). Experimental and numerical study on shear behavior of shear pockets between ultra-high-performance and normal concrete for precast girder bridges. In Structures (Vol. 55, pp. 1645-1658). Elsevier.

[17] Zhu, J. W., Pan, Y., Liu, J. P., Hassanein, M. F., & Li, H. T. (2025). Flexural Behavior of Steel-UHPC-NC Composite Girders with Different UHPC-NC Interface Treatments. Journal of Bridge Engineering, 30(7), 04025047.

[18] Shabani, H., Asadian, A., & Galal, K. (2025). Flexural and serviceability behaviour of macro-synthetic fibre-reinforced concrete beams reinforced with GFRP bars. Construction and Building Materials, 494, 143217.

[19] Lin, L., Tan, J., Zhang, C., Wu, X., Gu, F., Zou, C., ... & Lv, P. (2025). Tension stiffening behaviors of reinforced ultra-high performance concrete. Journal of Sustainable Cement-Based Materials, 14(9), 1825-1847.

[20] Yu, J., Yao, Y. Q., Lu, Y., & Liang, S. L. (2025). Experiments and combined microscopic and macroscopic simulations of out-of-plane behavior of one-way S-UHPC-S composite wall strips. Journal of Structural Engineering, 151(12), 04025199.

[21] Qiu, M., Cao, J., Shao, Z., Li, H., Qu, Z., Zhou, C., & Shao, X. (2025). Flexural cracking behavior of steel-NC-UHPC composite beam under negative bending moment. Engineering Structures, 322, 119071.

[22] Liu, C., Li, Y., Zhang, J., & Wan, D. (2026). Analysis of Flexural Performance and Crack Width Prediction Models of UHPC Composite Slabs. Buildings, 16(2), 411.

[23] Qiu, M., Cao, J., Shao, Z., Li, H., Qu, Z., Zhou, C., & Shao, X. (2025). Flexural cracking behavior of steel-NC-UHPC composite beam under negative bending moment. Engineering Structures, 322, 119071.

[24] Kazemi, F., Asgarkhani, N., Shafighfard, T., Jankowski, R., & Yoo, D. Y. (2025). Machine-learning methods for estimating performance of structural concrete members reinforced with fiber-reinforced polymers. Archives of computational methods in engineering, 32(1), 571-603.

[25] Thai, H. T. (2022, April). Machine learning for structural engineering: A state-of-the-art review. In Structures (Vol. 38, pp. 448-491). Elsevier.

[26] Azimi, M., Eslamlou, A. D., & Pekcan, G. (2020). Data-driven structural health monitoring and damage detection through deep learning: State-of-the-art review. Sensors, 20(10), 2778.

[27] Feng, D. C., Liu, Z. T., Wang, X. D., Chen, Y., Chang, J. Q., Wei, D. F., & Jiang, Z. M. (2020). Machine learning-based compressive strength prediction for concrete: An adaptive boosting approach. Construction and Building Materials, 230, 117000.

[28] Mangalathu, S., Hwang, S. H., & Jeon, J. S. (2020). Failure mode and effects analysis of RC members based on machine-learning-based SHapley Additive exPlanations (SHAP) approach. Engineering Structures, 219, 110927.

[29] Sapkota, S. C., Panagiotakopoulou, C., Dahal, D., Beskopylny, A. N., Dahal, S., & Asteris, P. G. (2025). Optimizing high-strength concrete compressive strength with explainable machine learning. Multiscale and Multidisciplinary Modeling, Experiments and Design, 8(3), 160.

[30] Sapkota, S. C., Panagiotakopoulou, C., Dahal, D., Beskopylny, A. N., Dahal, S., & Asteris, P. G. (2025). Optimizing high-strength concrete compressive strength with explainable machine learning. Multiscale and Multidisciplinary Modeling, Experiments and Design, 8(3), 160.

[31] Lubliner, J., Oliver, J., Oller, S., & Onate, E. (1989). A plastic-damage model for concrete. International Journal of solids and structures, 25(3), 299-326.

[32] Lee, J., & Fenves, G. L. (1998). Plastic-damage model for cyclic loading of concrete structures. Journal of engineering mechanics, 124(8), 892-900.

[33] Buttignol, T. E. T., Sousa, J. L. A. O., & Bittencourt, T. N. (2017). Ultra High-Performance Fiber-Reinforced Concrete (UHPFRC): a review of material properties and design procedures. Revista IBRACON de estruturas e materiais, 10(4), 957-971.

[34] Lemes, Í. J., Silveira, R. A., Silva, A. R., & Rocha, P. A. (2017). Nonlinear analysis of two-dimensional steel, reinforced concrete and composite steel-concrete structures via coupling SCM/RPHM. Engineering Structures, 147, 12-26.

[35] Savino, V., Lanzoni, L., Tarantino, A. M., & Viviani, M. (2020). A cohesive FE model for simulating the cracking/debonding pattern of composite NSC-HPFRC/UHPFRC members. Construction and Building Materials, 258, 119516.

[36] Su, Y. L., Wu, C., Shang, J. Q., Zhang, P., & Sheikh, S. A. (2024, January). Experimental and numerical simulation research on the flexural performance of beams reinforced with GFRP bars and three-sides UHPC layer. In Structures (Vol. 59, p. 105746). Elsevier.